

**This item is the archived peer-reviewed author-version of:**

Defect-limited thermal conductivity in MoS<sub>2</sub>

**Reference:**

Polanco C.A., Pandey Tribhuvan, Berlijn T., Lindsay L.- Defect-limited thermal conductivity in MoS<sub>2</sub>  
Physical review materials / American Physical Society - ISSN 2475-9953 - 4:1(2020), 014004  
Full text (Publisher's DOI): <https://doi.org/10.1103/PHYSREVMATERIALS.4.014004>  
To cite this reference: <https://hdl.handle.net/10067/1905100151162165141>

## Defect-limited thermal conductivity in MoS<sub>2</sub>

C. A. Polanco<sup>1</sup>, T. Pandey<sup>2</sup>, T. Berlijn<sup>3,4</sup>, and L. Lindsay<sup>1</sup>

<sup>1</sup>Materials Science and Technology Division, Oak Ridge National Laboratory, Oak Ridge, Tennessee 37831, USA

<sup>2</sup>Department of Physics, University of Antwerp, Groenenborgerlaan 171, B-2020 Antwerp, Belgium

<sup>3</sup>Center for Nanophase Materials Sciences, Oak Ridge National Laboratory, Oak Ridge, Tennessee 37831, USA

<sup>4</sup>Computational Sciences and Engineering Division, Oak Ridge National Laboratory, Oak Ridge, Tennessee 37831, USA

### *Abstract*

The wide measured range of thermal conductivities ( $k$ ) for monolayer MoS<sub>2</sub> and corresponding incongruent calculated values in the literature all suggest that extrinsic defect thermal resistance is significant and varied in synthesized samples of this material. Here we present defect-mediated thermal transport calculations of MoS<sub>2</sub> using interatomic forces derived from density functional theory combined with Green's function methods to describe phonon-point-defect interactions and a Peierls-Boltzmann formalism for transport. Conductivity calculations for bulk and monolayer MoS<sub>2</sub> using different density functional formalisms are compared. Non-perturbative first principles methods are used to describe defect-mediated spectral functions, scattering rates, and phonon  $k$ , particularly from Sulfur vacancies ( $V_S$ ), and in the context of the plethora of measured and calculated literature values. We find that  $k$  of monolayer MoS<sub>2</sub> is sensitive to phonon- $V_S$  scattering in the range of experimentally observed densities, and that first principles  $k$  calculations using these densities can explain the range of

measured values found in the literature. Furthermore, measured  $k$  values for bulk MoS<sub>2</sub> are more consistent because V<sub>S</sub> defects are not as prevalent.

## I. INTRODUCTION

Transition metal dichalcogenides, MoS<sub>2</sub> in particular, have enjoyed strong attention in basic and applications-based research, partly because monolayers can be easily cleaved from the corresponding bulk materials, like graphene, and partly because they are tuneable bandgap semiconductors (depending on layer thickness), unlike graphene. Vibrational properties and lattice thermal transport can play critical roles in determining limitations and functionalities of potential applications. For example, as electronic devices shrink toward the nanoscale, power densities vastly increase and thermal management is a key factor for improved device performance.

An abundance of experimental [1-19] and theoretical [20-38] investigations have examined thermal transport and its underlying vibrational properties in bulk, multilayer, and monolayer MoS<sub>2</sub> only to raise a variety of questions, including: What is the role of defects and size in limiting thermal conductivity ( $k$ )? How do different synthesis and characterization techniques lead to quantitatively different  $k$  values in these systems? What interatomic descriptions best describe the phonon interactions that govern  $k$  behavior? To illustrate these questions, **Figure 1** compiles a variety of calculated and measured room temperature (RT)  $k$  values from the literature and compares with our calculations for bulk and monolayer RT in-plane  $k$  as a function of sample size (calculation details are given in **Section II**). As long mean free path phonons carry a significant portion of heat in monolayer and van der Waals (vdW) layered materials  $k$  values can be sensitive to size effects even at RT. Measured in-plane multilayer and bulk MoS<sub>2</sub> RT  $k$  values range from 30-35 W/m-K (thin films) [15, 19] to 110 W/m-K [5], while calculations range from ~80 W/m-K [31] to 390 W/m-K [34] (some anomalously low values from molecular dynamics simulations are neglected here). For monolayer MoS<sub>2</sub> the experimental range of RT

in-plane  $k$  values is 13 W/m-K [13] to 84 W/m-K [7], while the theoretical range for these is 20 W/m-K [27] to 400 W/m-K [24]. Generally, there is a large spread of calculated and measured  $k$  values for bulk and monolayer MoS<sub>2</sub>, and discrepancies among them that are not fully understood.

As measured and calculated  $k$  values vary significantly due to size effects (sample size and characterization techniques) and defects (including point defects, isotopes, and polymer residues), this article gives a synopsis of literature values in the context of our calculated values for both monolayer and bulk MoS<sub>2</sub>. We give a description of vibrational and transport properties in these systems from density functional theory (DFT) calculations, comparing values obtained from the local density approximation (LDA) and the generalized gradient approximation (GGA). More importantly, we describe phonon-defect-limited  $k$  in monolayer MoS<sub>2</sub> fully from first principles Green's function methods to understand discrepancies between measured and calculated  $k$  values. Dilute Sulfur vacancies ( $V_S$ ) provide significant thermal resistance for heat-carrying phonons, and calculations here are compared with previous work considering much larger defect densities [28].

In **Section II**, intrinsic vibrational properties and transport behaviors of MoS<sub>2</sub> systems are discussed in the context of DFT-derived Peierls-Boltzmann transport [39-41]. **Section III** gives a description of the DFT-derived Green's function method [42-44] used for describing defect-limited thermal transport. **Section IV** summarizes this work.

## II. INTRINSIC PHONONS AND CONDUCTIVITY

DFT-derived Peierls-Boltzmann transport has been discussed in great detail in a variety of previous works [45-49]. Details specific to the MoS<sub>2</sub> calculations are provided here.

*Calculation details* – Calculations of structural parameters [in-plane lattice constant ( $a$ ), cross-plane lattice constant ( $c$ ) [bulk only], and distance between consecutive S layers ( $d_{S-S}$ )] and interatomic force constants [harmonic (phonons) and anharmonic (three-phonon interactions)] were derived from DFT using the Quantum Espresso (QE) package [50]. Electronic structure calculations for monolayer MoS<sub>2</sub> used 13x13x1 k-integration meshes, an 80 Ry plane wave energy cutoff, Martins-Troullier (MT) pseudopotentials [51] to represent the core electrons, and a vacuum space between layers  $\sim 15$  Å resulting in:  $a=3.190$  Å and  $d_{S-S}=3.147$  Å for GGA (Perdew-Burke-Ernzerhof exchange and correlations [52]) and  $a=3.091$  Å and  $d_{S-S}=3.097$  Å for LDA (Perdew-Wang (PW) exchange and correlations [53]). As reported in the supplemental material of our previous work [19], a 6x6x6 k-integration mesh, 70 Ry plane wave energy cutoff, MT pseudopotentials, LDA-PW exchange and correlations for bulk MoS<sub>2</sub> (no vacuum space needed) give:  $a=3.094$  Å,  $c=12.069$  Å, and  $d_{S-S}=3.099$  Å.

Harmonic and anharmonic IFCs of MoS<sub>2</sub> were determined by numerical differentiation built from forces calculated on sets of 9x9x1 supercells (243 atoms) with appropriate atoms perturbed by 0.03 Å from their equilibrium positions. A cutoff of  $\sim 9.75$  Å ( $\sim 5.60$  Å) was used to truncate the harmonic (anharmonic) IFCs. Translational invariance of the anharmonic IFCs was enforced by slightly altering the irreducible IFC set (those not related by symmetries of the crystal structure and derivative permutation) using a  $\chi^2$  minimization procedure described in previous work [54, 55]. A similar procedure was employed for the manipulation of the harmonic IFCs, however, additionally including rotational invariance [56, 57] and Born-Huang equilibrium constraints [57, 58]. These ensure that the low-frequency behavior of the flexure acoustic (ZA) branch is quadratic [58, 59]. The inset in **Figure 2** shows calculations of the ZA branch of monolayer MoS<sub>2</sub> using uncorrected harmonic IFCs [negative frequency values (imaginary

phonons)] compared with these using symmetry-corrected IFCs (quadratic curve). Further details regarding IFC calculations for bulk MoS<sub>2</sub> are given in Ref. [19]. QE input files, harmonic IFCs, and anharmonic IFCs are given in the supplemental information [60]; other information can be provided upon request.

*Phonons and  $k$*  – The LDA calculated in-plane lattice parameter for monolayer MoS<sub>2</sub> is ~3% smaller than the GGA calculated values. This discrepancy is typical [61] and translates into harder phonons predicted by the LDA. **Figure 2** gives the phonon dispersions for monolayer MoS<sub>2</sub>, both LDA and GGA, along high symmetry directions and compared with available measured data and the LDA calculated dispersion for bulk MoS<sub>2</sub>. For the lowest acoustic frequencies the variations in the dispersions predicted by the LDA and GGA are small; however, for the optic branches and higher acoustic frequencies variations are apparent. Harder acoustic phonons have generally larger velocities ( $\vec{v}_{\vec{q}j}$ ) for these heat-carrying modes and higher optic phonon branches tend to reduce acoustic-optic phonon couplings giving larger transport lifetimes ( $\tau_{\vec{q}j\alpha}$ ). Here,  $\vec{q}$  is the wave vector,  $j$  is the polarization, and  $\alpha$  is the Cartesian direction for a particular phonon mode.

Since the thermal conductivity is given by:

$$k_{\alpha} = \sum_{\vec{q}j} C_{\vec{q}j} v_{\vec{q}j\alpha}^2 \tau_{\vec{q}j\alpha} \quad (1)$$

larger velocities and lifetimes give larger  $k$ . **Equation 1** is a sum over all phonon modes in the first Brillouin zone and  $C_{\vec{q}j} = (\hbar\omega_{\vec{q}j})^2 n_{\vec{q}j}^0 (n_{\vec{q}j}^0 + 1) / k_B T^2$  is the mode heat capacity with  $n_{\vec{q}j}^0$  the Bose-Einstein distribution and  $\omega_{\vec{q}j}$  the phonon frequency. Generally,  $k$  is a tensor; however, for monolayer MoS<sub>2</sub>  $k$  is described by a single parameter for in-plane transport and the layer thickness is defined as 6.033 Å, the distance between bulk MoS<sub>2</sub> layers [22]. For bulk MoS<sub>2</sub>,  $k$  is

described by separate in-plane and cross-plane components. Cross-plane  $k$  is not considered in this work. All  $k$  calculations here include three-phonon interactions and phonon-isotope scattering from naturally-occurring isotope concentrations (14.65%  $^{92}\text{Mo}$ , 9.19%  $^{94}\text{Mo}$ , 15.87%  $^{95}\text{Mo}$ , 16.67%  $^{96}\text{Mo}$ , 9.58%  $^{97}\text{Mo}$ , 24.29%  $^{98}\text{Mo}$ , and 9.75%  $^{100}\text{Mo}$ , 94.99%  $^{32}\text{S}$ , 0.75%  $^{33}\text{S}$ , 4.25%  $^{34}\text{S}$ , 0.01%  $^{36}\text{S}$ ) derived from quantum perturbation theory [63-65]. Size dependence was determined by including phonon-boundary scattering rates of the empirical form  $1/\tau_{\vec{q}i}^b = 2|v_{\vec{q}i\alpha}|/L$  where  $\alpha$  is taken along the transport direction. Details of phonon- $V_s$  scattering are given in the next section. From these scattering rates the transport lifetimes are calculated by self-consistently solving the Peierls-Boltzmann transport equation to determine the non-equilibrium phonon distributions [66-68]. Here, the extrinsic defect scattering rates are treated within the relaxation time approximation (RTA) [40, 41, 67].

As demonstrated in **Figure 1**, LDA  $k$  values calculated here for monolayer  $\text{MoS}_2$  are higher than those from the GGA (178 and 143 W/m-K at RT, respectively). In general, this is also true of the calculated literature values in **Figure 1**, though with significant spread. We note that there are many more GGA  $k$  calculations than LDA reported in the literature for monolayer  $\text{MoS}_2$ . For bulk  $k_{\text{in}}$ , the opposite is true, more LDA calculations exist, and both LDA and GGA give more consistent results. To verify the robustness of our calculations, independent GGA monolayer  $k$  calculations were performed using combined VASP [69], Phonopy [70], and Phono3py simulation packages [71]. Here, an 18 Å vacuum and 520 eV (~38 Ry) energy cutoff give  $a=3.176$  Å. Harmonic IFCs were calculated from 9x9x1 supercells using  $\Gamma$ -point only calculations. Anharmonic IFCs were similarly calculated though with 7x7x1 supercells and truncated interactions at 6.75 Å. For the  $k$  calculations a 55x55x1 integration grid was used with delta functions in phonon-phonon matrix elements approximated by an adaptive Gaussian

function with a smearing parameter of 1.0 [71]. From this method the calculated monolayer  $k$  is 127 W/m-K, ~10% lower than our other GGA calculation.

Measured  $k_{\text{in}}$  values for bulk MoS<sub>2</sub> span a large range of values; however, considering the largest values over the range of system sizes available, theory gives a good description of the experiments. This suggests that for the lower measured values other extrinsic effects may be providing significant thermal resistance, e.g., point defects or uncharacterized grain boundaries. All measured  $k$  values for monolayer MoS<sub>2</sub> lie well below our calculations (both LDA and GGA), most other calculations, and below the highest bulk measurements. This is surprising as interlayer interactions are expected to reduce in-plane  $k$  for bulk as compared with monolayer systems, as found in calculations. The cause for these discrepancies may derive from phonon scattering from defects and surface residues for which monolayer systems may be more sensitive. Defect-limited  $k$  of monolayer MoS<sub>2</sub> is examined in the next section.

### III. EXTRINSIC PHONON-DEFECT INTERACTIONS

Defects in bulk and monolayer MoS<sub>2</sub> have been intensively explored [72-75], particularly related to their effects on thermal transport [11, 18, 19], electronic transport [76], and photoluminescence excitations [77, 78]. Among the variety of possible point defects (e.g., vacancy complexes, adatoms, vacancies, antisite defects) the most prevalent in monolayer MoS<sub>2</sub> synthesized by chemical vapor deposition or mechanical exfoliation are single Sulfur vacancies (V<sub>s</sub>) [72, 73] with average concentrations estimated  $\sim 1.2 \times 10^{13} \text{ cm}^{-2}$  (a bit shy of 1%) and ranging from  $0.5$  to  $3.5 \times 10^{13} \text{ cm}^{-2}$  [72]. Previous first principles calculations have demonstrated that vacancies, even at low concentrations, can provide significant thermal resistance in a variety of materials as they strongly perturb the crystal via mass variation, restructuring around the vacancy center, and resulting force constant variations [79-82]. In fact, recent first principles calculations

have demonstrated a large reduction in  $k$  of monolayer MoS<sub>2</sub> [28], though for periodic defect distributions and concentrations significantly higher than found in experiments, as they were limited by supercell size. Thus, here we study defect-limited  $k$  of MoS<sub>2</sub> with Sulfur vacancies and Sulfur adatoms in the dilute limit using Green's function techniques.

To describe phonon-defect scattering we use a non-perturbative T-matrix methodology with harmonic IFCs from DFT supercells of perfect monolayer MoS<sub>2</sub> and from those with a single defect as inputs. This technique has been described in previous work [43, 79-83]; only details relevant to monolayer MoS<sub>2</sub> are presented here. IFC calculations for phonon-defect interactions are similar to those described above for the harmonic IFCs, though using 7x7x1 supercells (147 atoms) with atomic perturbations of 0.04 Å and including interactions to nineteenth nearest neighbors (up to 9.87 Å in the perfect system). **We only considered neutral defects here and note that a spectroscopic study as well as theoretical calculations found that V<sub>S</sub> defects can switch between neutral and -1 charge states [84, 85]. Forces were relaxed within 0.0005 Ry Bohr<sup>-1</sup> for the single defect supercell in a series of calculations. First, the defect and nearest neighbor atoms were allowed to freely relax to new equilibrium positions while keeping all other atoms fixed. The next relaxation calculation allowed the defect, nearest neighbors, and second nearest neighbors to find relaxed positions. Progressively more neighboring shells were included in a series of calculations until all atoms in the supercell obtained new relaxed equilibrium positions. After relaxation, atoms around the V<sub>S</sub> contract. In particular, the first neighbor distance shrinks from 2.422 Å to 2.387 Å for the S atom on the opposite side of the monolayer with respect to the vacancy. On the other hand, atoms around the S adatom slightly expand. The distance from the S atom just below the S adatom to its first nearest neighbors increases from 2.422 Å to 2.427 Å. Moreover, the distance between the adatom and its nearest neighbor is 1.939 Å. The relaxed**

atomic equilibrium positions for the defect supercells are given in QE input files in the supplemental information [60]. The differences in harmonic IFCs from the perfect and defect supercells build into the T-matrix and resulting phonon-defect scattering rates [43, 79-83]. These scattering rates are included in the Peierls-Boltzmann transport equation within the RTA, similar to phonon-isotope and phonon-boundary scattering.

Before examining defect-limited  $k$ , **Figure 3** demonstrates the mode broadening induced by phonon- $V_S$  interactions in monolayer MoS<sub>2</sub>, though beyond the dilute limit here with  $V_S$  density  $22.7 \times 10^{13} \text{ cm}^{-2}$  (10% of Sulfur atoms) for better visualization of the influence of disorder on the calculated phonon structure. This spectral function is configurationally averaged using an effective disordered Hamiltonian method [86, 87]. Similar to the Green's function method described above, an impurity potential is defined by the difference of harmonic IFCs with and without a single  $V_S$ . From this, twenty different effective Hamiltonians are constructed for supercells with an average of 560 atoms and 40 randomly located  $V_S$  defects (and varying supercell shapes), each with density  $\sim 22.7 \times 10^{13} \text{ cm}^{-2}$ , by removing the force constants corresponding to the missing Sulfur atoms and adjusting the remaining IFCs according to the calculated  $V_S$  impurity potential. Following the unfolding formula of Ref. 88 atomically resolved spectral functions for each randomly configured supercell are computed by exact diagonalization of the constructed Hamiltonians. These are averaged to give the spectral dispersion of **Figure 3**. For each disordered supercell construction, IFCs were altered to ensure that restoring forces on each atom were equal and opposite to the induced forces on the other atoms (Newton's third law); otherwise, spurious imaginary frequencies are present. Not surprisingly, the disorder broadens the phonon bands in momentum space and frequency space, corresponding to finite mean free paths and lifetimes induced by scattering of the phonons by  $V_S$  disorder. Significant

broadening occurs for acoustic modes in the ~5 and ~6 THz regions (see **Figure 3**) where the bands are flattened and more susceptible to disorder-induced phonon scattering. This is qualitatively consistent with the results obtained from the T-matrix method (scattering rates in **Figure 5**).

Including phonon- $V_S$  interactions (from the Green's function description) with defect densities estimated from experiment severely reduces the calculated  $k$  of monolayer MoS<sub>2</sub>. The inset to **Figure 4** gives the GGA calculated RT  $k$  of monolayer MoS<sub>2</sub> as a function of  $V_S$  density and scaled by  $k$  with no phonon- $V_S$  scattering. Also shown are calculated RT  $k$  as a function of Sulfur adatom density. We find that adatoms provide significantly stronger thermal resistance, particularly for lower frequency phonons (see **Figure 5**); however, the literature does not suggest that these defects have comparable densities to those found for  $V_S$  defects. The green box denotes the range of  $V_S$  densities observed in measurements, while the green circle gives the average  $V_S$  concentration [72]. The range of observed  $V_S$  densities corresponds to the largest variance in  $k$  via phonon- $V_S$  scattering, from 20% to 70% of its intrinsic value. This defect

sensitivity may be the primary reason for the diversity of measured monolayer MoS<sub>2</sub>  $k$  values in the literature.

Also shown in Figure 4 are two calculated monolayer MoS<sub>2</sub>  $k$  values including Sulfur vacancies with large defect densities from Ref. 28. It is not clear why these calculated  $k$  values are much larger than those predicted here; however, we highlight three important calculation differences. First, the defect densities are large enough for defect correlations [89] to become non-negligible. We consider randomly distributed isolated defects, while Ref. 28 considers periodically ordered V<sub>S</sub>. Second, the 3x3x1 supercells (27 atoms) that made the calculations in Ref. 28 tractable are quite small. This may lead to spurious supercell interactions that can stiffen the vibrational frequencies and give higher  $k$ . Third, the defect supercells in Ref. 28 were not relaxed after incorporating each V<sub>S</sub> in the perfect system. Local distortions around vacancies after relaxation were shown to provide important thermal resistance in diamond [79] and graphene [81]. In graphene, these distortions gave enhanced phonon-defect scattering particularly at higher vacancy concentrations (see Figure 13(c) of Ref. [81]).

**Figure 6** gives the GGA calculated  $k$  of monolayer MoS<sub>2</sub> including phonon-V<sub>S</sub> scattering as a function of system size. The dark gray curve corresponds to the average V<sub>S</sub> concentration, while the gray area gives the calculated  $k$  for the concentration range of 0.5 (top of area) to 3.5 (bottom of area) x10<sup>13</sup> cm<sup>-2</sup>. Using the same phonon-V<sub>S</sub> scattering rates (determined from GGA supercells) with the LDA  $k$  calculation shifts this gray area upward the same difference found between the LDA and GGA  $k$  calculations in **Figure 1** (~15%). Indeed, the defect-mediated  $k$  calculations cover the observed range of measured monolayer MoS<sub>2</sub>  $k$  values barring a single data point with a very low value [13]. This strongly suggests that these V<sub>S</sub> vacancies play a critical role in thermal transport and are the primary driver for observed discrepancies among

experiments and when comparing with theoretical results. Furthermore, better general agreement between the highest measurements and calculations of  $k$  for bulk MoS<sub>2</sub> (see **Figure 1**) likely occurs because observed estimated V<sub>S</sub> densities range from 0.007 to 0.03 x10<sup>13</sup> cm<sup>-2</sup> [74, 75] in bulk, orders of magnitude smaller than those in monolayer MoS<sub>2</sub>.

The severe reduction of thermal conductivity via Sulfur vacancies follows from its relatively large scattering strength. **Figure 5** gives the calculated three-phonon (at RT), phonon-V<sub>S</sub> (density 1.2x10<sup>13</sup> cm<sup>-2</sup>), phonon-S-adatom (same defect density), phonon-isotope (natural S and Mo isotope abundances), and phonon-boundary ( $L=5\mu\text{m}$ ) scattering rates for the six lowest frequency branches including the acoustic phonons. At higher frequencies phonon-isotope scattering is comparable to the anharmonic and phonon-V<sub>S</sub> scattering rates, while at very low frequencies the boundary scattering becomes important. However, for this set of parameters, the anharmonic and phonon-V<sub>S</sub> scatterings provide more significant thermal resistance, and their scattering rates have very similar magnitudes over the acoustic frequency range. Thus, the monolayer MoS<sub>2</sub>  $k$  is sensitive to the defect density in the experimentally observed density range. **Sulfur adatoms are particularly effective at scattering low frequency acoustic phonons and thus may provide strong thermal resistance similar to phonon-V<sub>S</sub> scattering even for lower defect concentrations.**

For lower (higher) temperatures the anharmonic scattering rates decrease (increase), while the defect-mediated scattering rates are insensitive to temperature. Thus, at higher temperatures defects provide less relative resistance, while at low temperatures these mechanisms become dominant. For this reason, temperature-dependent  $k$  measurements can provide important information regarding thermal resistance mechanisms in particular MoS<sub>2</sub> samples. **Figure 7** gives calculated  $k$  for bulk (LDA) and monolayer (GGA) MoS<sub>2</sub> as a function of temperature and

compared with available measured data for monolayer MoS<sub>2</sub>. Surprisingly few measured temperature-dependent  $k$  values exist for monolayer MoS<sub>2</sub>: a series of measurements on a supported sample [6] and two series with suspected surface residues and small grain sizes  $\sim 0.5$   $\mu\text{m}$  [11]. Measured  $k$  values presented in **Figure 1** and **Figure 6** correspond to RT experiments. All measured curves demonstrate behavior inconsistent with the  $T^{-1}$   $k$  dependence of purely three-phonon scattering at higher temperatures. The supported sample gives  $\sim T^{-5}$  temperature dependence, while the suspended samples are nearly temperature independent for  $T > 150\text{K}$ . Further temperature-dependent  $k$  measurements on high quality monolayer MoS<sub>2</sub> samples are required to better understand its intrinsic  $k$  behavior and relation to extrinsic defects.

#### IV. SUMMARY

This work presented defect-limited thermal conductivity calculations of MoS<sub>2</sub> systems from DFT-derived Peierls-Boltzmann transport and Green's function methodologies in the context of the plethora of theoretical and measured values in the literature. Different density functional approximations were compared and the effects of Sulfur vacancies on vibrational spectral functions and size- and temperature-dependent  $k$  of monolayer MoS<sub>2</sub> were examined. In particular, we find that monolayer  $k$  values are sensitive to phonon- $V_S$  scattering in the range of densities observed in experiments. This sensitivity can explain the wide range of measured monolayer MoS<sub>2</sub>  $k$  values in the literature and discrepancies found with theory. Furthermore, measurements and calculations of  $k$  for bulk MoS<sub>2</sub> are more consistent due to its having significantly less  $V_S$  densities.

#### V. ACKNOWLEDGEMENTS

This work was supported by the US Department of Energy, Office of Science, Office of Basic Energy Sciences, Material Sciences and Engineering Division. Computational resources were

provided by the National Energy Research Scientific Computing Center (NERSC), a DOE Office of Science User Facility supported by the Office of Science of the US Department of Energy under Contract No. DE-AC02-05CH11231.

## Figure Captions

**Figure 1:** Calculated (colors) and measured (black) room temperature  $k$  of monolayer and multilayer/bulk MoS<sub>2</sub> as a function of characteristic size. Curves represent calculated data generated here, while symbols are literature values [1-38] (numbers give references for some values, measured monolayer values can be found in **Figure 6**). The dashed curve and open symbols correspond to in-plane multilayer/bulk values, while the solid curves and filled symbols correspond to monolayer MoS<sub>2</sub>  $k$ . Note that the number of layers or layer thickness is not distinguished here. For the calculations, green corresponds to LDA values, red corresponds to GGA values, and purple corresponds to empirical potential descriptions of the interatomic interactions. ‘Size’ is estimated by the average lateral sample dimensions (length and width) or characterization method for measured  $k$ , e.g., diameter of laser spot size in thermo-reflectance measurements or hole in supporting substrate in Raman thermometry measurements. For calculated literature values a ‘size’ is given, while here size is determined by  $L$  described in the text. Calculations of  $k$  with no sample size (or ‘infinite’ size) are reported here at 100  $\mu\text{m}$ .

**Figure 2:** Calculated phonon dispersions of monolayer (solid curves) and bulk (dashed curves) MoS<sub>2</sub> compared with measured data for monolayer (purple diamonds; Raman [18]) and bulk (black circles; neutrons [62]) MoS<sub>2</sub>. Green corresponds to LDA calculations, while red corresponds to GGA. **Inset:** Uncorrected low frequency dispersion of the flexure acoustic branch of monolayer MoS<sub>2</sub> using a 9x9 supercell (purple imaginary curve). The red curve corresponds to the symmetry-corrected dispersion, while the dashed green curve corresponds to the lowest frequency in-plane transverse acoustic branch of bulk MoS<sub>2</sub>.

**Figure 3:** Configurationally averaged disordered spectral dispersion of monolayer MoS<sub>2</sub> with  $V_S$  density  $22.7 \times 10^{13} \text{ cm}^{-2}$  (10% Sulfur atoms missing) with blue/red intensity corresponding to the Mo/S weight.

**Figure 4:** GGA calculated  $k$  of monolayer MoS<sub>2</sub> as a function of  $V_S$  (red curve) and S adatom (blue curve) density. The green box denotes the range of  $V_S$  densities found in Ref. 72 (0.5 to  $3.5 \times 10^{13} \text{ cm}^{-2}$ ), while the green circle gives the estimated average  $V_S$  density of  $1.2 \times 10^{13} \text{ cm}^{-2}$ . The black diamonds are calculated values from Ref. 28 for  $V_S$  densities of 12.6 and  $25.2 \times 10^{13} \text{ cm}^{-2}$ . The inset demonstrates the S adatom (blue) configuration above the top layer of Sulfur atoms (yellow).

**Figure 5:** GGA calculated phonon scattering rates for the six lowest frequency branches of monolayer MoS<sub>2</sub>: three-phonon interactions at RT (black circles), phonon- $V_S$  scattering with density of  $1.2 \times 10^{13} \text{ cm}^{-2}$  (red circles), phonon-S-adatom scattering with the same density, phonon-isotope scattering with natural Sulfur and Molybdenum concentrations (purple circles), and phonon-boundary scattering with  $L=5 \mu\text{m}$  (green circles).

**Figure 6:** GGA calculated  $k$  of monolayer MoS<sub>2</sub> compared with RT measurements (numbers label references) as a function of size. The red curve and measured data (black squares) are the same as in **Figure 1**. The dark gray curve corresponds to the GGA calculated monolayer MoS<sub>2</sub>  $k$  including  $1.2 \times 10^{13} \text{ cm}^{-2}$  Sulfur vacancies (average estimated density in Ref. 72), while the gray area represents the range of  $k$  with  $V_S$  densities between  $0.5 \times 10^{13} \text{ cm}^{-2}$  and  $3.5 \times 10^{13} \text{ cm}^{-2}$  (range from Ref. 72). The inset shows a defect structure: Molybdenum atoms (purple), Sulfur atoms (yellow), and Sulfur vacancy (red).

**Figure 7:** Calculated  $k$  of bulk (dashed green curve) and monolayer (solid red and purple curves) MoS<sub>2</sub> as a function of temperature. Symbols represent measured MoS<sub>2</sub>  $k$  data:

black squares (bulk [12]), orange circles (supported monolayers [6]), and purple and blue circles (suspended monolayers [11]). The solid red and dashed green curves include anharmonic, phonon-isotope (natural isotope concentrations), and phonon-boundary ( $L=10\mu\text{m}$ ) interactions. The solid purple curve includes anharmonic, phonon-isotope (natural isotope concentrations), phonon-boundary ( $L=0.5\mu\text{m}$ ), and phonon- $V_S$  ( $1.2 \times 10^{13} \text{ cm}^{-2}$ ) interactions.

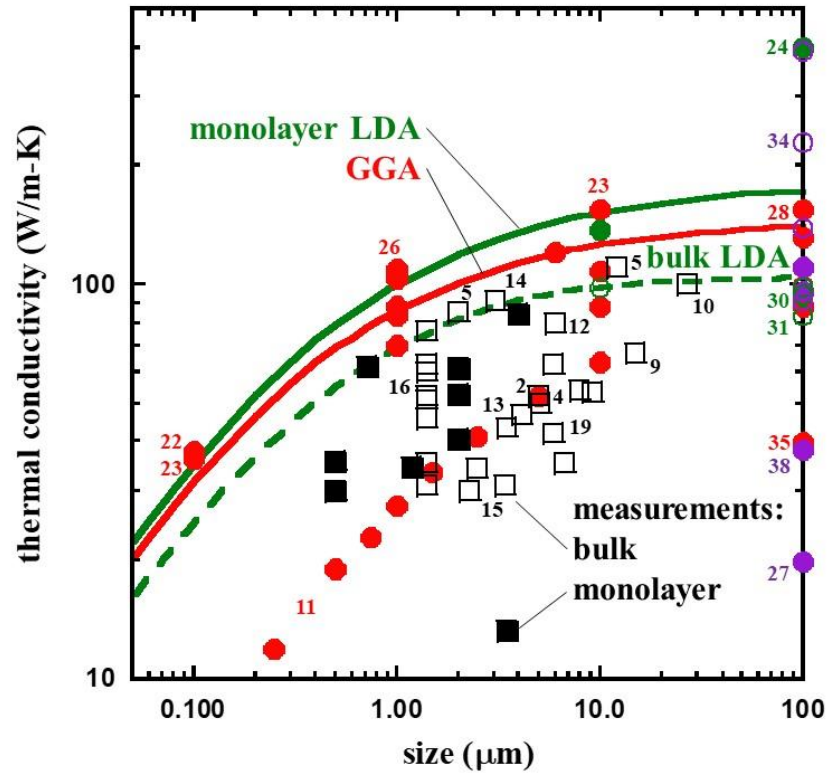


Figure 1

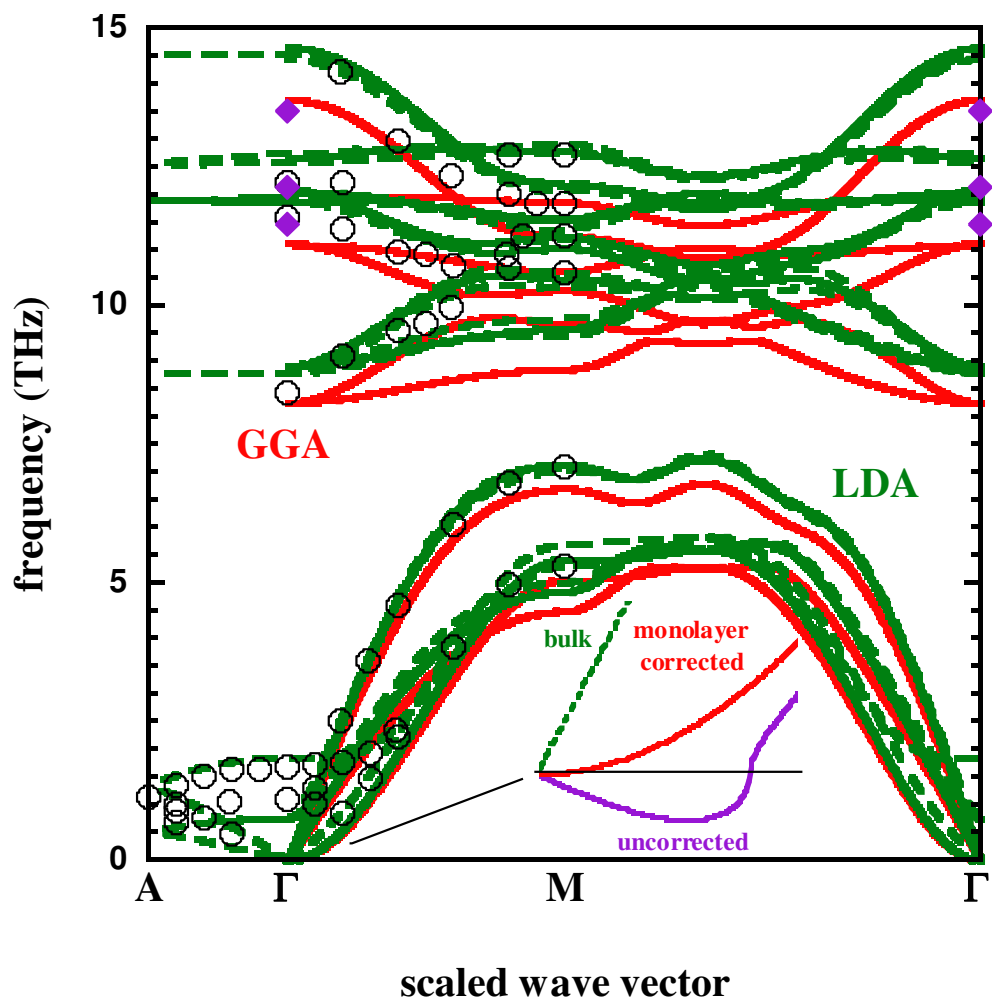
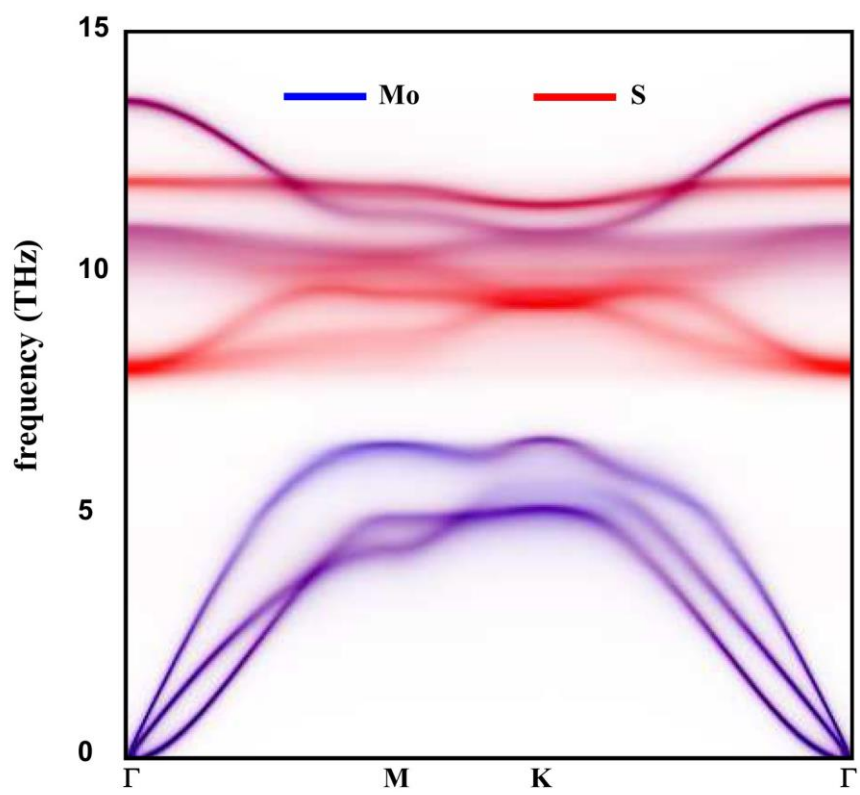


Figure 2



**Figure 3**

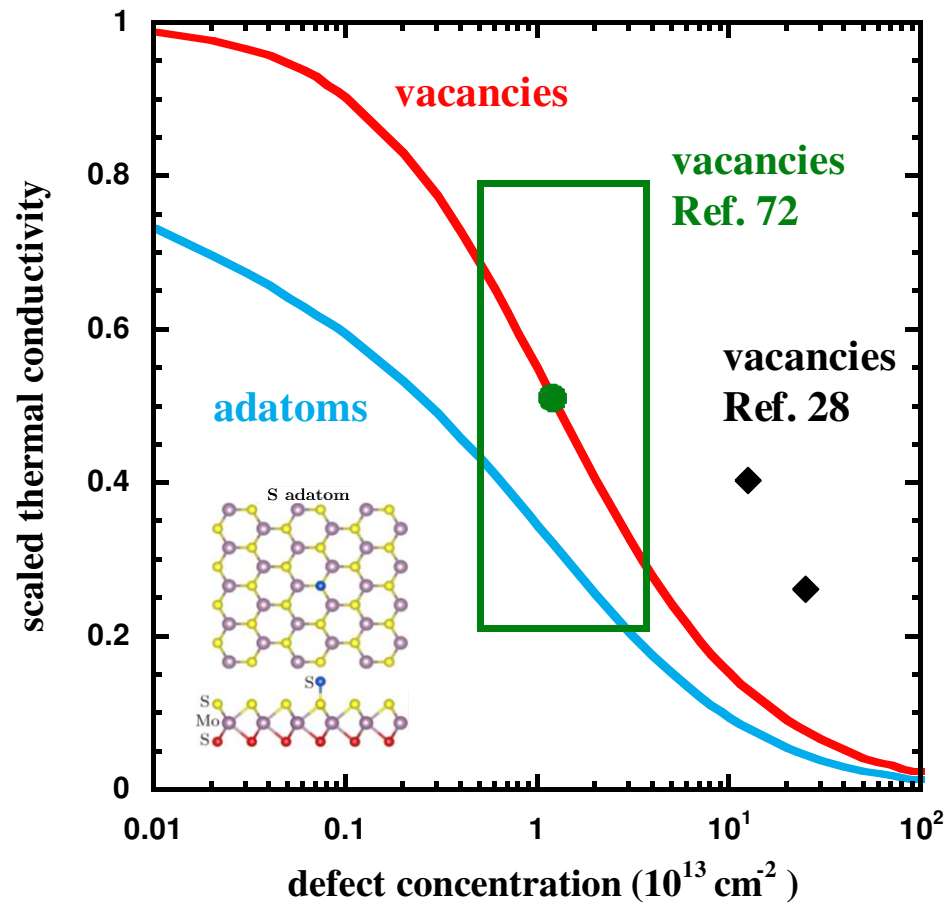


Figure 4

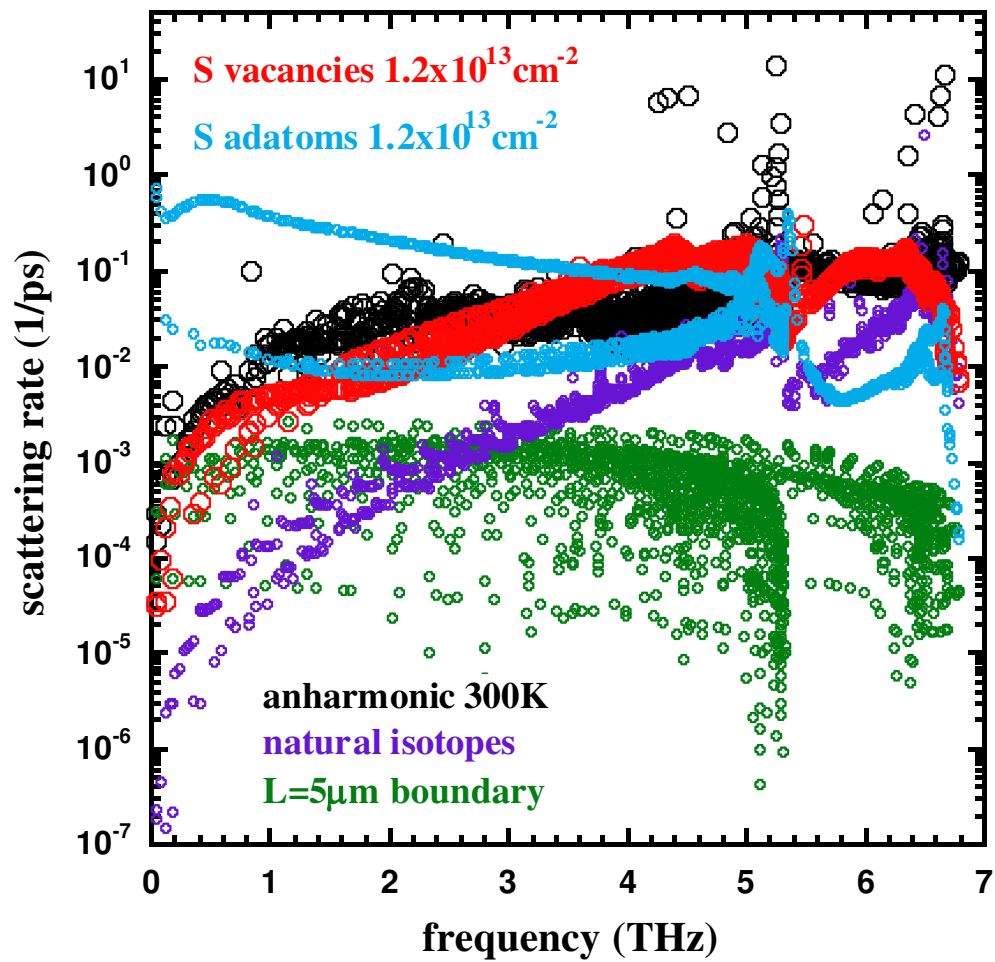


Figure 5

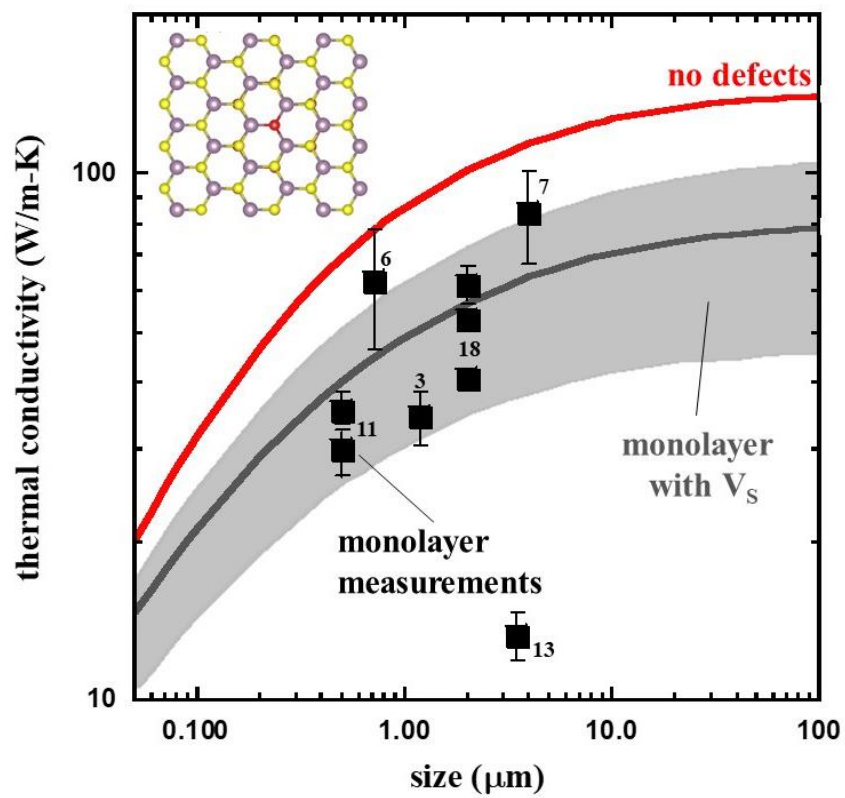


Figure 6

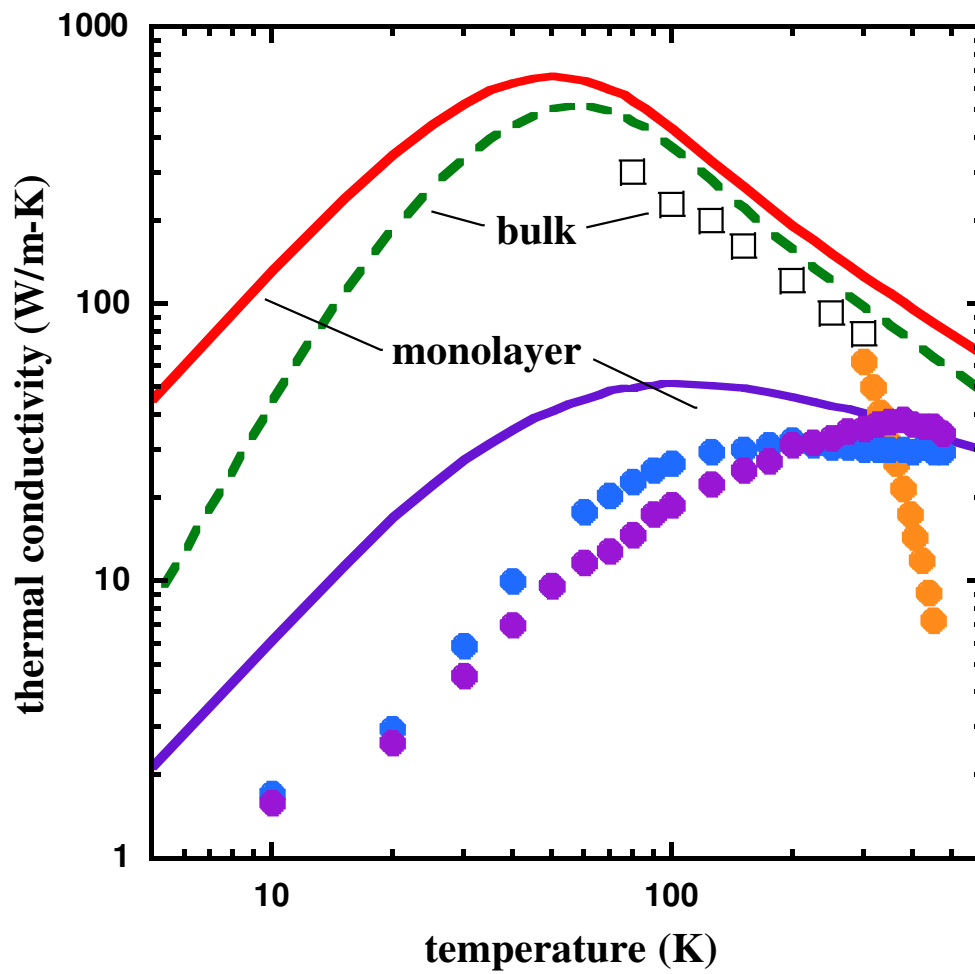


Figure 7

## References

- [1] C. Lee, H. Yan, L. E. Brus, T. F. Heinz, J. Hone, and S. Ryu, "Anomalous lattice vibrations of single- and few-layer MoS<sub>2</sub>," ACS Nano 4, 2695 (2010).
- [2] S. Sahoo, A. P. S. Gaur, M. Ahmadi, M. J.-F. Guinel, and R. S. Katiyar, "Temperature-dependent Raman studies and thermal conductivity of few-layer MoS<sub>2</sub>," J. Phys. Chem. C 117, 9042 (2013).
- [3] R. Yan, J. R. Simpson, S. Bertolazzi, J. Brivio, M. Watson, X. Wu, A. Kis, T. Luo, A. R. H. Walker, and H. G. Xing, "Thermal conductivity of monolayer molybdenum disulfide obtained from temperature-dependent Raman spectroscopy," ACS Nano 8, 986 (2014).
- [4] I. Jo, M. T. Pettes, E. Ou, W. Wu, and L. Shi, "Basal-plane thermal conductivity of few-layer molybdenum disulfide," Appl. Phys. Lett. 104, 201902 (2014).
- [5] J. Liu, G.-M. Choi, and D. G. Cahill, "Measurement of the anisotropic thermal conductivity of molybdenum disulfide by the time-resolved magneto-optic Kerr effect," J. Appl. Phys. 116, 233107 (2014).
- [6] A. Taube, J. Judek, A. Łapińska, and M. Zdrojek, "Temperature-dependent thermal properties of supported MoS<sub>2</sub> monolayers," ACS Appl. Mat. Interfaces 7, 5061 (2015).
- [7] X. Zhang, D. Sun, Y. Li, G.-H. Lee, X. Cui, D. Chenet, Y. You, T. F. Heinz, and J. C. Hone, "Measurement of lateral and interfacial thermal conductivity of single- and bilayer MoS<sub>2</sub> and MoSe<sub>2</sub> using refined optothermal Raman technique," ACS Appl. Mat. Interfaces 7, 25923 (2015).
- [8] A. Pisoni, J. Jacimovic, O. S. Barišić, A. Walter, B. Náfrádi, P. Bugnon, A. Magrez, H. Berger, Z. Revay, and L. Forró, "The role of transport agents in MoS<sub>2</sub> single crystals," J. Phys. Chem. C 119, 3918 (2015).

- [9] J. Judek, A. P. Gertych, M. Świniarski, A. Łapińska, A. Dużyńska, and M. Zdrojek, “High accuracy determination of the thermal properties of supported 2D materials,” *Sci. Rep.* 5, 12422 (2015).
- [10] G. Zhu, J. Liu, Q. Zheng, R. Zhang, D. Li, D. Banerjee, and D. G. Cahill, “Tuning thermal conductivity in molybdenum disulfide by electrochemical intercalation,” *Nat. Commun.* 7, 13211 (2016).
- [11] M. Yarali, X. Wu, T. Gupta, D. Ghoshal, L. Xie, Z. Zhu, H. Brahmi, J. Bao, S. Chen, T. Luo, N. Koratkar, and A. Mavrokefalos, “Effects of defects on the temperature-dependent thermal conductivity of suspended monolayer molybdenum disulfide grown by chemical vapor deposition,” *Adv. Funct. Mat.* 27, 1704357 (2017).
- [12] P. Jiang, X. Qian, X. Gu, and R. Yang, “Probing anisotropic thermal conductivity of transition metal dichalcogenides  $\text{MX}_2$  ( $\text{M}=\text{Mo}$ ,  $\text{W}$  and  $\text{X}=\text{S}$ ,  $\text{Se}$ ) using time-domain thermoreflectance,” *Adv. Mat.* 29, 1701068 (2017).
- [13] J. J. Bae, H. Y. Jeong, G. H. Han, J. Kim, H. Kim, M. S. Kim, B. H. Moon, S. C. Lim, and Y. H. Lee, “Thickness-dependent in-plane thermal conductivity of suspended  $\text{MoS}_2$  grown by chemical vapor deposition,” *Nanoscale* 9, 2541 (2017).
- [14] M. Goni, J. Yang, and A. J. Schmidt, “Enhanced thermal transport across monolayer  $\text{MoS}_2$ ,” *Nano Research* 11, 2173 (2018).
- [15] A. Aiyiti, S. Hu, C. Wang, Q. Xi, Z. Cheng, M. Xia, Y. Ma, J. Wu, J. Guo, Q. Wang, J. Zhou, J. Chen, X. Xu, and B. Li, “Thermal conductivity of suspended few-layer  $\text{MoS}_2$ ,” *Nanoscale* 10, 2727 (2018).

- [16] P. Yuan, R. Wang, T. Wang, X. Wang, and Y. Xie, "Nonmonotonic thickness-dependence of in-plane thermal conductivity of few-layered MoS<sub>2</sub>: 2.4 to 37.8 nm," *Phys. Chem. Chem. Phys.* 20, 25752 (2018).
- [17] X. Meng, T. Pandey, J. Jeong, S. Fu, J. Yang, K. Chen, A. Singh, F. He, X. Xu, J. Zhou, W.-P. Hsieh, A. K. Singh, J.-F. Lin, and Y. Wang, "Thermal conductivity enhancement in MoS<sub>2</sub> under extreme strain," *Phys. Rev. Lett.* 122, 155901 (2019).
- [18] X. Li, J. Zhang, A. A. Puretzky, A. Yoshimura, X. Sang, Q. Cui, Y. Li, L. Liang, A. W. Ghosh, H. Zhao, R. R. Unocic, V. Meunier, C. M. Rouleau, B. G. Sumpter, D. B. Geohegan, and K. Xiao, "Isotope-engineering the thermal conductivity of two-dimensional MoS<sub>2</sub>," *ACS Nano* 12, 2481 (2019).
- [19] B. Smith, L. Lindsay, J. Kim, E. Ou, R. Huang, and L. Shi, "Phonon interaction with ripples and defects in thin layered molybdenum disulfide," *Appl. Phys. Lett.* 114, 221902 (2019).
- [20] V. Varshney, S. S. Patnaik, C. Muratore, A. K. Roy, A. A. Voevodin, and B. L. Farmer, "MD simulations of molybdenum disulphide (MoS<sub>2</sub>): Force-field parameterization and thermal transport behavior," *Comp. Mat. Sci.* 48, 101 (2010).
- [21] X. Liu, G. Zhang, Q.-X. Pei, and Y.-W. Zhang, "Phonon thermal conductivity of monolayer MoS<sub>2</sub> sheet and nanoribbons," *Appl. Phys. Lett.* 103, 133113 (2013).
- [22] W. Li, J. Carrete, and N. Mingo, "Thermal conductivity and phonon linewidths of monolayer MoS<sub>2</sub> from first principles," *Appl. Phys. Lett.* 103, 253103 (2013).
- [23] X. Gu and R. Yang, "Phonon transport in single-layer transition metal dichalcogenides: A first-principles study," *Appl. Phys. Lett.* 105, 131903 (2014).
- [24] A. Cepellotti, G. Fugallo, L. Paulatto, M. Lazzeri, F. Mauri, and N. Marzari, "Phonon hydrodynamics in two-dimensional materials," *Nat. Commun.* 6, 6400 (2015).

- [25] Z. Ding, Q.-X. Pei, J.-W. Jiang, and Y.-W. Zhang, "Manipulating the thermal conductivity of monolayer MoS<sub>2</sub> via lattice defect and strain engineering," *J. Phys. Chem. C* 119, 16358 (2015).
- [26] L. Zhu, T. Zhang, Z. Sun, J. Li, G. Chen, and S. A. Yang, "Thermal conductivity of biaxial-strained MoS<sub>2</sub>: Sensitive strain dependence and size-dependent reduction rate," *Nanotechnology* 26, 465707 (2015).
- [27] Z. Ding, J.-W. Jiang, Q.-X. Pei, and Y.-W. Zhang, "In-plane and cross-plane thermal conductivities of molybdenum disulfide," *Nanotechnology* 26, 065703 (2015).
- [28] B. Peng, Z. Ning, H. Zhang, H. Shao, Y. Xu, G. Ni, and H. Zhu, "Beyond perturbation: Role of vacancy-induced localized phonon states in thermal transport of monolayer MoS<sub>2</sub>," *J. Phys. Chem. C* 120, 29342 (2016).
- [29] X. Gu, B. Li, and R. Yang, "Layer thickness-dependent phonon properties and thermal conductivity of MoS<sub>2</sub>," *J. Appl. Phys.* 119, 085106 (2016).
- [30] A. N. Gandi and U. Schwingenschlögl, "Thermal conductivity of bulk and monolayer MoS<sub>2</sub>," *Euro. Phys. Lett.* 113, 36002 (2016).
- [31] D. O. Lindroth and P. Erhart, "Thermal transport in van der Waals solids from first-principles calculations," *Phys. Rev. B* 94, 115205 (2016).
- [32] B. Peng, H. Zhang, H. Shao, Y. Xu, X. Zhang, and H. Zhu, "Towards intrinsic phonon transport in single-layer MoS<sub>2</sub>," *Ann. Phys.* 528, 504 (2016).
- [33] X. Wang and A. Tabarraei, "Phonon thermal conductivity of monolayer MoS<sub>2</sub>," *Appl. Phys. Lett.* 108, 191905 (2016).

- [34] K. Xu, A. J. Gabourie, A. Hashemi, Z. Fan, N. Wei, A. B. Farimani, H.-P. Komsa, A. V. Krasheninnikov, E. Pop, and T. Ala-Nissila, “Thermal transport in MoS<sub>2</sub> from molecular dynamics using different empirical potentials,” *Phys. Rev. B* 99, 054303 (2019).
- [35] J.-J. Ma, J.-J. Zheng, X.-L. Zhu, P.-F. Liu, W.-D. Li, and B.-T. Wang, “First-principles calculations of thermal transport properties in MoS<sub>2</sub>/MoSe<sub>2</sub> bilayer heterostructure,” *Phys. Chem. Chem. Phys.* 21, 10442 (2019).
- [36] S. Chen, A. Sood, E. Pop, K. E. Goodson, and D. Donadio, “Strongly tunable anisotropic thermal transport in MoS<sub>2</sub> by strain and lithium intercalation: First-principles calculations,” *2D Materials* 6, 025033 (2019).
- [37] A. Kandemir, H. Yapicioglu, A. Kinaci, T. Çağın, and C. Sevik, “Thermal transport properties of MoS<sub>2</sub> and MoSe<sub>2</sub> monolayers,” *Nanotechnology* 27, 055703 (2016).
- [38] A. Krishnamoorthy, P. Rajak, P. Norouzzadeh, D. J. Singh, R. K. Kalia, A. Nakano, and P. Vashishta, “Thermal conductivity of MoS<sub>2</sub> monolayers from molecular dynamics simulations,” *AIP Advances* 9, 035042 (2019).
- [39] R. E. Peierls, “On the kinetic theory of thermal conduction in crystals,” *Ann. Phys.* 395, 1055 (1929).
- [40] J. M. Ziman, *Electrons and Phonons* (Oxford University Press, London, 1960).
- [41] G. P. Srivastava, *The Physics of Phonons* (Taylor and Francis Group, New York, 1990).
- [42] E. N. Economou, *Green’s Functions in Quantum Physics*, 3<sup>rd</sup> ed. (Springer, Berlin, 2006).
- [43] N. Mingo, K. Esfarjani, D. A. Broido, and D. A. Stewart, “Cluster scattering effects on phonon conduction in graphene,” *Phys. Rev. B* 81, 045408 (2010).
- [44] A. Kundu, N. Mingo, D. A. Broido, and D. A. Stewart, “Role of light and heavy embedded nanoparticles on the thermal conductivity of SiGe alloys,” *Phys. Rev. B* 84, 125426 (2011).

- [45] D. A. Broido, M. Malorny, G. Birner, N. Mingo, and D. A. Stewart, "Intrinsic lattice thermal conductivity of semiconductors from first principles," *Appl. Phys. Lett.* 91, 231922 (2007).
- [46] L. Lindsay, "First principles Peierls-Boltzmann phonon thermal transport: A topical review," *Nanoscale and Microscale Thermophysical Eng.* 20, 67 (2016).
- [47] L. Lindsay, C. Hua, X. L. Ruan, and S. Lee, "Survey of ab initio phonon thermal transport," *Materials Today Phys.* 7, 106 (2018).
- [48] A. J. H. McGaughey, A. Jain, H.-Y. Kim, and B. Fu, "Phonon properties and thermal conductivity from first principles, lattice dynamics, and the Boltzmann transport equation," *J. Appl. Phys.* 125, 011101 (2019).
- [49] L. Lindsay, A. Katre, A. Cepellotti, and N. Mingo, "Perspective on ab initio phonon thermal transport," *J. Appl. Phys.* 126, 050902 (2019).
- [50] P. Giannozzi, S. Baroni, N. Bonini, M. Calandra, R. Car, C. Cavazzoni, D. Ceresoli, G. L. Chiarotti, M. Cococcioni, I. Dabo, A. D. Corso, S. Gironcoli, S. Fabris, G. Fratesi, R. Gebauer, U. Gerstmann, C. Gougoussis, A. Kokalj, M. Lazzeri, L. Martin-Samos *et al.*, "QUANTUM ESPRESSO: A modular and open-source software project for quantum simulations of materials," *J. Phys.: Condens. Matter* 21, 395502 (2009).
- [51] N. Troullier and J. L. Martins, "Efficient pseudopotentials for plane-wave calculations," *Phys. Rev. B* 43, 1993 (1991).
- [52] J. P. Perdew, K. Burke, and M. Ernzerhof, "Generalized gradient approximation made simple," *Phys. Rev. Lett.* 77, 3865 (1996).
- [53] J. P. Perdew and Y. Wang, "Pair-distribution function and its coupling-constant average for the spin-polarized electron gas," *Phys. Rev. B* 46, 12947 (1992).

- [54] L. Lindsay, D. A. Broido, and T. L. Reinecke, "Ab initio thermal transport in compound semiconductors," *Phys. Rev. B* 87, 165201 (2013).
- [55] N. Mingo, D. A. Stewart, D. A. Broido, L. Lindsay, and W. Li, in *Length-Scale Dependent Phonon Interactions*, edited by S. L. Shinde and G. P. Srivastava (Springer, New York, 2014).
- [56] D. C. Gazis and R. F. Wallis, "Conditions for rotational invariance of a harmonic lattice," *Phys. Rev.* 151, 578 (1966).
- [57] M. Born and K. Huang, *Dynamical Theory of Crystal Lattices* (Clarendon, Oxford, 1954).
- [58] H. Fan, H. Wu, L. Lindsay, and Y. Hu, "Ab initio investigation of single-layer high thermal conductivity boron compounds," *Phys. Rev. B* 100, 085420 (2019).
- [59] J. Carrete, W. Li, L. Lindsay, D. A. Broido, L. J. Gallego, and N. Mingo, "Physically founded phonon dispersions of few-layer materials and the case of borophene," *Mater. Res. Lett.* 4, 204 (2016).
- [60] Supplemental information includes QE input files, harmonic IFCs, anharmonic IFCs, and QE input files for relaxed defect supercells.
- [61] P. Haas, F. Tran, and P. Blaha, "Calculation of the lattice constant of solids with semilocal functionals," *Phys. Rev. B* 79, 085104 (2009).
- [62] N. Wakabayashi, H. G. Smith, and R. M. Nicklow, "Lattice dynamics of hexagonal MoS<sub>2</sub> studied by neutron scattering," *Phys. Rev. B* 12, 659 (1975).
- [63] S. I. Tamura, "Isotope scattering of dispersive phonons in Ge," *Phys. Rev. B* 27, 858 (1983).
- [64] S. I. Tamura, "Isotope scattering of large-wave-vector phonons in GaAs and InSb: Deformation-dipole and overlap-shell models," *Phys. Rev. B* 30, 849 (1984).

- [65] L. Lindsay, D. A. Broido, and T. L. Reinecke, “Phonon-isotope scattering and thermal conductivity in materials with a large isotope effect: A first-principles study,” *Phys. Rev. B* 88, 144306 (2013).
- [66] M. Omini and A. Sparavigna, “Beyond the isotropic-model approximation in the theory of thermal conductivity,” *Phys. Rev. B* 53, 9064 (1996).
- [67] L. Lindsay, D. A. Broido, and N. Mingo, “Flexural phonons and thermal transport in graphene,” *Phys. Rev. B* 82, 115427 (2010).
- [68] L. Lindsay and C. A. Polanco, “Thermal transport by first-principles anharmonic lattice dynamics,” book chapter in *Handbook of Materials Modeling*, eds: W. Adreoni and S. Yip, pg. 1-31 (Springer, Cham, Switzerland, 2018).
- [69] G. Kresse and J. Furthmüller, “Efficiency of ab-initio total energy calculations for metals and semiconductors using a plane-wave basis set,” *Comp. Mat. Sci.* 6, 15 (1996).
- [70] A. Togo and I. Tanaka, “First principles phonon calculations in materials science,” *Scripta Materialia* 108, 1 (2015).
- [71] A. Togo, L. Chaput, and I. Tanaka, “Distributions of phonon lifetimes in Brillouin zones,” *Phys. Rev. B* 91, 094306 (2015).
- [72] J. Hong, Z. Hu, M. Probert, K. Li, D. Lv, X. Yang, L. Gu, N. Mao, Q. Feng, L. Xie, J. Zhang, D. Wu, Z. Zhang, C. Jin, W. Ji, X. Zhang, J. Yuan, and Z. Zhang, “Exploring atomic defects in molybdenum disulphide monolayers,” *Nat. Commun.* 6, 6293 (2015).
- [73] W. Zhou, X. Zou, S. Najmaei, Z. Liu, Y. Shi, J. Kong, J. Lou, P. M. Ajayan, B. I. Yakobson, and J.-C. Idrobo, “Intrinsic structural defects in monolayer molybdenum disulfide,” *Nano Lett.* 13, 2615 (2013).

- [74] C.-P. Lu, G. Li, J. Mao, L.-M. Wang, and E. Y. Andrei, “Bandgap, mid-gap states, and gating effects in MoS<sub>2</sub>,” *Nano Lett.* 14, 4628 (2014).
- [75] F. D. Brandão, G. M. Ribeiro, P. H. Vaz, J. C. González, and K. Krambrock, “Identification of rhenium donors and sulfur vacancy acceptors in layered MoS<sub>2</sub> bulk samples,” *J. Appl. Phys.* 119, 235701 (2016).
- [76] H. Qiu, Z. Wang, W. Ren, H. Nan, Z. Ni, Q. Chen, S. Yuan, F. Miao, F. Song, G. Long, Y. Shi, L. Sun, J. Wang, and X. Wang, “Hopping transport through defect-induced localized states in molybdenum disulphide,” *Nat. Commun.* 4, 2642 (2013).
- [77] S. Tongay, J. Suh, C. Ataca, W. Fan, A. Luce, J. S. Kang, J. Liu, C. Ko, R. Raghunathanan, J. Zhou, F. Ogletree, J. Li, J. C. Grossman, and J. Wu, “Defects activated photoluminescence in two-dimensional semiconductors: Interplay between bound, charged, and free excitons,” *Sci. Rep.* 3, 2657 (2013).
- [78] H. Nan, Z. Wang, W. Wang, Z. Liang, Y. Lu, Q. Chen, D. He, P. Tan, F. Miao, X. Wang, J. Wang, and Z. Ni, “Strong photoluminescence enhancement of MoS<sub>2</sub> through defect engineering and oxygen bonding,” *ACS Nano* 8, 5738 (2014).
- [79] N. A. Katcho, J. Carrete, W. Li, and N. Mingo, “Effect of nitrogen and vacancy defects on the thermal conductivity of diamond: An ab initio Green’s function approach,” *Phys. Rev. B* 90, 094117 (2014).
- [80] N. H. Protik, J. Carrete, N. A. Katcho, N. Mingo, and D. Broido, “Ab initio study of the effect of vacancies on the thermal conductivity of boron arsenide,” *Phys. Rev. B* 94, 045207 (2016).
- [81] C. A. Polanco and L. Lindsay, “Ab initio phonon point defect scattering and thermal transport in graphene,” *Phys. Rev. B* 97, 014303 (2018).

[82] C. A. Polanco and L. Lindsay, “Thermal conductivity of InN with point defects from first principles,” *Phys. Rev. B* 98, 014306 (2018).

[83] E. N. Economou, *Green’s Functions in Quantum Physics*, 3<sup>rd</sup> Ed. (Springer, Berlin, 2006).

[84] S. H. Song, M.-K. Joo, M. Neumann, H. Kim, and Y. H. Lee, “Probing defect dynamics in monolayer MoS<sub>2</sub> via noise nanospectroscopy,” *Nat. Commun.* 8, 2121 (2017).

[85] H.-P. Komsa and A. V. Krasheninnikov, “Native defects in bulk and monolayer MoS<sub>2</sub> from first principles,” *Phys. Rev. B* 91, 125304 (2015).

[86] T. Berlijn, D. Volja, and W. Ku, “Can disorder alone destroy the e’<sub>g</sub> hole pockets of Na<sub>x</sub>CoO<sub>2</sub>? A Wannier function based first-principles method for disordered systems,” *Phys. Rev. Lett.* 106, 077005 (2011).

[87] O. Delaire, I. I. Al-Qasir, A. F. May, C. W. Li, B. C. Sales, J. L. Niedziela, J. Ma, M. Matsuda, D. L. Abernathy, and T. Berlijn, “Heavy-impurity resonance, hybridization, and phonon spectral functions in Fe<sub>1-x</sub>M<sub>x</sub>Si (M=Ir, Os),” *Phys. Rev. B* 91, 094307 (2015).

[88] W. Ku, T. Berlijn, and C.-C. Lee, “Unfolding first-principles band structures,” *Phys. Rev. Lett.* 104, 216401 (2010).

[89] I. Savić, N. Mingo, and D. A. Stewart, “Phonon transport in isotope-disordered carbon and boron-nitride nanotubes: Is localization observable?” *Phys. Rev. Lett.* 101, 165502 (2008).

~~[87] T. Berlijn, C. H. Lin, W. Garber, and W. Ku, “Do transition metal substitutions dope carriers in iron-based superconductors?” *Phys. Rev. Lett.* 108, 207003 (2012).~~